

# Learning Cross-Scale Visual Representations for Real-Time Image Geo-Localization

Tianyi Zhang<sup>1</sup>, Matthew Johnson-Roberson<sup>1</sup>

**Abstract**— Robot localization remains a challenging task in GPS denied environments. State estimation approaches based on local sensors, e.g. cameras or IMUs, are drifting-prone for long-range missions as error accumulates. In this study, we aim to address this problem by localizing image observations in a 2D multi-modal geospatial map. We introduce the cross-scale dataset and a methodology to produce additional data from cross-modality sources. We propose a framework that learns cross-scale visual representations without supervision. Experiments are conducted on data from two different domains, underwater and aerial. In contrast to existing studies in cross-view image geo-localization, our approach a) performs better on smaller-scale multi-modal maps; b) is more computationally efficient for real-time applications; c) can serve directly in concert with state estimation pipelines. Our code and data are released at <https://github.com/tyz1030/CroScaleRep.git>

**Index Terms**—Marine robotics, Representation Learning, Deep Learning for Visual Perception

## I. INTRODUCTION

GEO-LOCALIZATION plays a key role in autonomous and robotic systems exploring a priori unknown environments in the wild. To achieve better localization accuracy, a wide range of sensors have been used on today’s field robots. According to the reference frame, sensors can be generally categorized as local or global. Local sensors, e.g. cameras and inertial measurement units (IMUs), observe the environment in a local coordinate frame. Global sensors, e.g. global positioning systems (GPS), barometers, and magnetometers, provide global measurements in fixed global frames. While local sensors give high-precision local measurements, global sensors are noisier but do not suffer from the same drift effects when localizing the vehicle. The algorithmic combination of both kinds of sensors achieves locally accurate and globally drift-free performance on long-range tasks [1].

However, there are many scenarios where global information is not available or only partially available. The scenarios can be underwater, underground, or other GPS denied environments. Taking underwater as an example, neither GPS nor

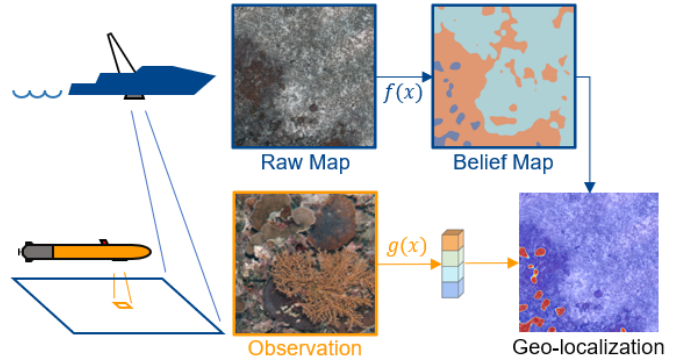


Fig. 1: Cross-scale<sup>i</sup> geo-localization: Small-scale raw map and large-scale image observation are encoded into probabilistic representations. Location of the image observation can then be inferred in the map.

land-based station towers can be accessed since electromagnetic waves are heavily attenuated. Acoustic localization gets downgraded by variation in salinity or temperature in the water body. Magnetometer and depth sensors are reliable global sensors underwater, however, they only provide measurements up to 4 degrees of freedom (DOFs) in total. The global measurements of the most important 2 DOFs on the horizontal plane are missing anyway.

The absence of global sensing has raised a global challenge for geo-localization: the incremental state estimation based on local-only sensor systems, i.e. dead reckoning, is prone to drifts which accumulate with time. Hence, in long-range missions, we need to find an approach to control the growing localization error online.

In this study, we conceive a real-time geo-localization system (see Fig. 1) for robot platforms equipped with RGB cameras. In this system, a 2D geospatial map is encoded into a belief map. Observations from the camera are encoded into feature representations and its 2D location can be inferred in the belief map. The key problem we address in this study is how to encode 2D geospatial maps of various modalities and image observations into consistent representations. The contributions of this study are as follows:

- We formulate the cross-scale<sup>i</sup> geo-localization task, which can help robots with large-scale image observations navigate in small-scale maps.
- We propose a workflow to sample cross-scale visual data from cross-modality resources. We build and release two datasets from different domains.
- We propose to use a pixels-to-pixels map encoder to

Manuscript received: September, 9, 2021; Revised January, 3, 2022; Accepted January, 31, 2022.

This paper was recommended for publication by Pauline Pounds upon evaluation of the Associate Editor and Reviewers’ comments.

<sup>1</sup>T. Zhang and M. Johnson-Roberson are with the Robotics Institute and the Department of Naval Architecture and Marine Engineering, University of Michigan, Ann Arbor, MI 48109, USA {tyz, mattjr}@umich.edu

Digital Object Identifier (DOI): see top of this page.

<sup>i</sup>Elsewhere in the literature *scale* usually refers to the size of the dataset. However throughout this paper, we use *scale* to refer to the geospatial scale (*pixel/m*) of maps or image observations. *Cross-scale* means that that the dataset contains maps of small scale and image observations of large scale.

efficiently encode map patches with small scale.

- We propose a framework which trains a map encoder and an image observation encoder jointly without supervision. We use Bhattacharyya coefficient [2] as the similarity metric between the probabilistic outputs of both encoders. We modified NT-Xent [3] as loss function for our case.
- We propose to use Dirichlet distribution to model the probability of encoded observation in an encoded map, which can be potentially leveraged in downstream inference applications.

## II. RELATED WORK

### A. Terrain-aided navigation (TAN) with particle filtering

Navigating an autonomous underwater vehicle (AUV) with a terrain elevation map has been studied for decades. Early work was conducted on an AUV equipped with single-point sonar and water depth sensor [4]. Since acquiring information from a map is a highly non-linear operation, a particle filter method is applied to TAN for state estimation. Subsequent work improved the TAN method by plugging in different kinds of range sensors [5], [6], upgrading the particle filter into different variants [7]–[9], developing efficient mapping features [10]–[12], and realizing cooperative TAN with multiple vehicles [13]–[15]. However, the success of a TAN system requires sufficient excitation from terrain elevation, which is not always guaranteed in many scenarios.

In our work, we break the limitation of using range sensors and a terrain elevation map. Instead, we explore the possibility of using RGB cameras as sensors, and maps of different modalities which provide richer geospatial information.

### B. Cross-view image geo-localization

Cross-view image geo-localization refers to determining the geolocation of a query image with an overhead satellite image. This problem was first formulated as an information retrieval problem in ground-and-overhead image databases and was attempted based on the extraction and matching of hand-crafted features [16]. Workman et al. [17] and Vo and Hays [18] approached this problem with convolutional neural network (CNN) backbones for different views and evaluated the performance of different training strategies and embedding architectures. Hu et al. [19] proposed CVM-Net which embedded the NetVLAD layer [20] on top of a CNN to extract descriptors invariant to viewpoint changes. Other extensive studies [21]–[23] developed domain transfer methods to bridge the gap between different viewpoints, but only apply to the cases that query image is panoramic.

Methods developed in this field of study are all based on the end-to-end framework of information retrieval and ranking. This makes it difficult to integrate such systems in TAN or other general Simultaneous Localization And Mapping (SLAM) workflow, which are mostly based on filtering and optimization. Moreover, the exhaustive sliding window search lacks the efficiency to deploy on the mobile platforms need real-time localization in a dynamically updating map.

In our study, we move away from the information retrieval framework and develop solutions more efficient and compatible for real-time geo-localization.

### C. Remote sensing (RS) image classification

Studies in RS image classification have inspired us with the feature association problem. Cao et al. [24] introduced a land use classification network with both aerial and street view images integrated. Street view features are interpolated by geo-coordinates and concatenated with aerial features. Hong et al. [25] proposed feature fusion and network training strategies for the multi-modal and cross-modal RS image classification. Above mentioned approaches both need supervision from ground truth labels to train.

### D. Contrastive learning

Recent progress in contrastive learning has shown how CNNs learn visual representations without supervision [3], [26]. Further, Pielawski et al. [27] proposed contrastive multimodal image representation for registration framework (CoMIR) which addressed the multimodal image registration problem with contrastive learning. However, CoMIR works with different modalities of exactly the same scale, which means that it is not directly applicable to our localization problem which has a large scale ratio between image observations and the map.

## III. PROBLEM FORMULATION

We aim to address the geo-localization problem with RGB image observations and multi-modal maps referenced in 2D geo-coordinates. RGB camera provides rich visual information and is one of the most affordable and widely-equipped perceptual sensors on mobile robots. However, high-resolution RGB satellite images which serve as maps in existing studies have limited coverage on the earth. We seek to exploit other lower-resolution modalities with smaller scale to serve as a map. In contrast to existing image geo-localization approaches, we focus on following goals:

- Localization in smaller-scale maps (typically, scale of an image observation has a magnitude of  $\times 10^1$  or larger than a map);
- Localization in maps of different modalities, which massively extend the data that can serve as maps;
- Efficient computation for real-time data processing;
- Compact map description for potentially efficient transmission over network;
- Compatibility as a plug-in module (instead of an end-to-end standalone program) in state estimation pipelines.

## IV. METHODOLOGY

### A. Cross-Scale Dataset

The basic data unit of our proposed cross-scale dataset is a data tuple, which consists of a 2D map patch  $M$ ,  $n$  image observations  $O = \{o_j\}_{j=1}^n$  and  $n$  pixel coordinates  $P = \{(u_j, v_j)\}_{j=1}^n$  indicating where elements of  $O$  are located in  $M$ . The whole dataset consists of a certain number of such data tuples sampled from one or multiple areas of interest.

Fig. 2 shows the workflow of sampling a data tuple  $(M, O, P)$ . First, we sample a map patch  $M$  with random coordinate and random rotation from the data source of small-scale map. Then we randomly sample  $P$  from map patch as

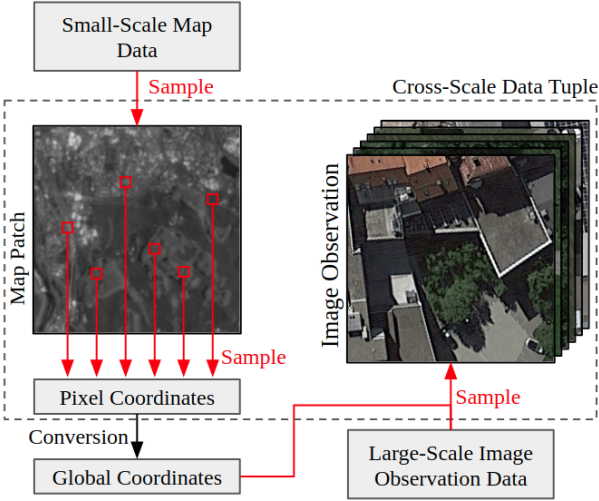


Fig. 2: Workflow of sampling the cross-scale dataset from data source of map and image observations. As the basic unit of our proposed dataset, a data tuple consists of a map patch, certain number of image observations and the pixel coordinates in the map patch where the center of image observations are located.

the centers where  $O$  will be sampled.  $P$  will be converted into global coordinates for sampling  $O$  from the data source of large-scale images.

### B. Network

The proposed network consists of a map encoder  $f$  and an observation encoder  $g$  to extract features from map patches and image observations (see Fig. 3).  $f$  encodes a map patch into a belief map, which has the same height and width with the input. The belief map has  $C$  channels, which corresponds to the  $C$  categories of terrain representations.  $g$  encodes the image into a 1D representation of size  $C$ . Both encoders are expected to learn representations consistent for the same location while distinguishable for different types of terrain.

Contrastive learning is applied for jointly training both encoders. For clarity, in this paper we use  $i$  to index data tuples in a minibatch, and  $j$  to index image observations and their corresponding pixel coordinates in one data tuple. Within a mini-batch  $B = \{(M_i, O_i, P_i)\}_{i=1}^b$  of size  $b$ , each map patch  $M_i$  is encoded into a belief map  $Z_i = f(M_i)$ . No matter how  $f$  is realized,  $\text{softmax}$  function as last layer will convert the output score of each pixel into a discrete probabilistic distribution. We expect that potential downstream applications do inference based on this property. The anchor feature  $z_{ij}$  is then extracted from  $Z_i$  by coordinate  $P_i$ , denoted by  $z_{ij} = Z_i[u_{ij}, v_{ij}]$ . Each image observation  $o_{ij}$  is first randomly augmented into 2 views,  $t^1(o_{ij})$  and  $t^2(o_{ij})$ , where  $t^1$  and  $t^2$  are different augmentation operators randomly sampled from same augmentation family. While various kinds of image augmentation has been recommended by [3], it's up to the task which augmentation will be applied in training. For example, color distortion can be necessary for underwater applications. Let  $y_{ij}^1 = g(t^1(o_{ij}))$  and  $y_{ij}^2 = g(t^2(o_{ij}))$  be the representations encoded from both augmented views. Similar

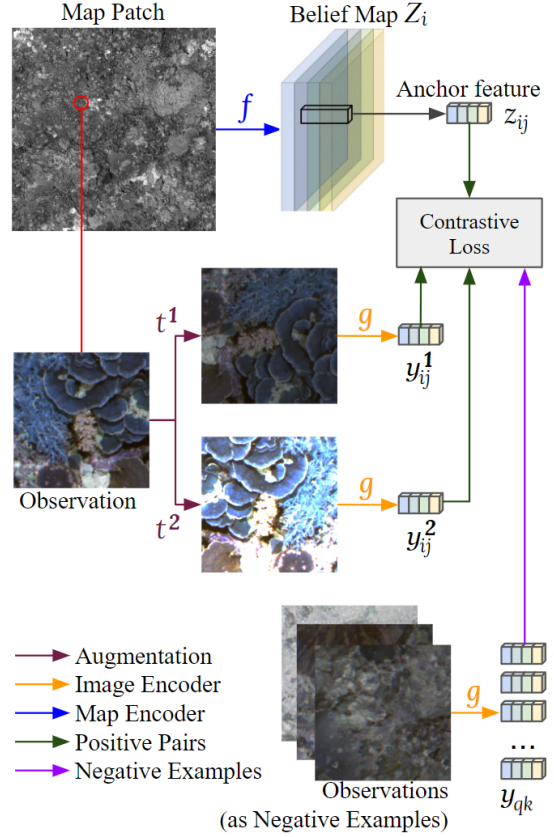


Fig. 3: The overview of our proposed framework. A map patch is encoded into a belief map. An image observation is augmented into two views then encoded into 1D representation. Anchor features are extracted from belief map by pixel coordinates. Image's representations and anchor features with corresponding pixel coordinates will serve as positive pairs and the rest of the images will be the negative examples.

to  $f$ ,  $\text{softmax}$  operation is applied as the last layer of  $g$ . Both  $y_{ij}^1$  and  $y_{ij}^2$  are considered as positive examples of the anchor feature  $z_{ij}$ . We treat augmented  $2(b \cdot n - 1)$  views of all the rest image observations in the mini-batch as negative examples.

### C. Similarity and Contrastive Loss

We adapt NT-Xent (the normalized temperature-scaled cross entropy loss) [3] to our case where one anchor feature has two positive examples. The loss function  $\mathcal{L}_{ij}$  for an anchor feature  $z_{ij}$  is defined as:

$$\mathcal{L}_{ij} = - \sum_{\lambda=1}^2 \log \frac{e^{s(z_{ij}, y_{ij}^{\lambda})/\tau}}{\sum_{q=1}^b \sum_{k=1}^n \sum_{\mu=1}^2 e^{s(z_{ij}, y_{qk}^{\mu})/\tau}} \quad (1)$$

where  $\tau$  is the temperature parameter [3].  $s(z, y)$  is the similarity function between  $z$  and  $y$ . Since the output after  $\text{softmax}$  layer are interpreted as discrete probabilistic distributions, we use Bhattacharyya coefficient [2] as the similarity function :

$$s(z, y) = \sqrt{z}^{\top} \sqrt{y} \quad (2)$$

where  $\sqrt{\cdot}$  performs element-wise operation. Though cosine similarity is widely used in well-proved contrastive learning

frameworks [3], [26], we do not use it in this work. Cosine similarity normalizes the encoder outputs before *softmax*, removing the ability to constrain the magnitude of the network activation. Such property will lead to inconsistent outputs between two encoders after *softmax*.

#### D. Inference

At location  $[u, v]$  (pixel coordinate in belief map), we want to find the distribution of observing representation  $y$  given  $Z[u, v]$  from belief map. We model the distribution of observed representation as a Dirichlet Distribution:

$$p(y|Z[u, v]) \sim \text{dirichlet}(\mathbf{1} + \theta Z[u, v]) \quad (3)$$

where  $\mathbf{1} = [1, \dots, 1, 1]$  has the same size with  $y$ .  $\theta$  is a free parameter to tune. Given an observed representation  $\hat{y}$ , The likelihood  $L([u, v], \hat{y})$  is modeled by:

$$L([u, v], \hat{y}) \propto p(y = \hat{y}|Z[u, v]) \quad (4)$$

which can be plugged into general SLAM frameworks. For example, Eq. 4 can be used to define the `NonlinearFactor` class as a measurement in the GTSAM framework [28].

## V. EXPERIMENTS

### A. Dataset

We build two datasets for this study, Scott Reef dataset and Kempton dataset. Each dataset contains 1000 data tuples to split for training and validation, and 200 data tuples for testing. For both datasets, we sample the image observation with the resolution of  $224 \times 224$  and the map patch with  $512 \times 512$ .

**Scott Reef dataset** is built from the Scott Reef 25 dataset (2009) [29] provided by Australian Centre for Field Robotics (ACFR). Since the raw Scott Reef data are images collected in a “lawn mowing” pattern without geo-tags, we use the 2D scene reconstruction map from the image sequence to generate the dataset for this study. The camera poses recovered with modern scene reconstruction techniques typically has a guaranteed accuracy and can serve as ground truth for studying localization problems [30]. Therefore, in the place of global geo-coordinates, we use the local geo-coordinate of the reconstruction map. The 2D RGB reconstruction covers an area of approximately  $100m \times 100m$  with the resolution  $50k \times 50k$ . Image observations are sampled from the raw-resolution reconstruction with  $\sim 500 \text{ pixel}/m$  scale. Map patches are sampled from the reconstruction down-scaled by a factor of  $\times 8$ , which has a scale of  $\sim 61 \text{ pixel}/m$ . With this dataset, we will show how our proposed method help robots improve localization over an area with map, which can play an important role on underwater robots surveying a pre-visited area or robot swarm streaming the map to each other. Potential cross-modality data (e.g. sonar scan or acoustic backscattering with global geo-tags) can be incorporated into our dataset by image registering [27] with the 2D reconstruction map.

**Kempton dataset** is built with the Sentinel-1 SAR [31] as map and Google Map Satellite [32] as image observations. Sentinel-1 data has a scale of  $0.1 \text{ pixel}/m$ , and 4 channels, i.e.  $vv$ ,  $vh$ ,  $hh$  and  $hv$ . We project the Sentinel-1 data using

Pseudo-Mercator (EPSG:3857) [31]. Google Map Satellite’s RGB images have a scale of  $\sim 7 \text{ pixels}/m$  with zoom level 20. Data are collected around  $longitude \in [10.22, 10.46]$  and  $latitude \in [47.62, 47.77]$ . We choose this area because of diverse terrain types and consistent satellite image quality.

### B. Implementation

First parameter to be determined is the size  $C$  of the output feature, which should be sufficient to describe the types of terrain in the dataset. Practically,  $C$  will be tuned as a hyperparameter in training. However, the magnitude of  $C$  can be predetermined with some human knowledge of terrain types. For example, if we believe the number of terrain types in the area of interest lies between 5 to 10, then this will be the range we use to tune the parameter.

We realize the map encoder with FCN-ResNet50 [33]. We define the last `conv2d` layer of `FCNHead` to output feature of  $C = 5$  channels. We add a `softmax` layer at the end of the network to convert the score map to the belief map. We choose ResNet18 [34] as the image encoder. Similarly, we have the FC layer to output representations of size  $C = 5$ , and add a `softmax` layer as the last layer.

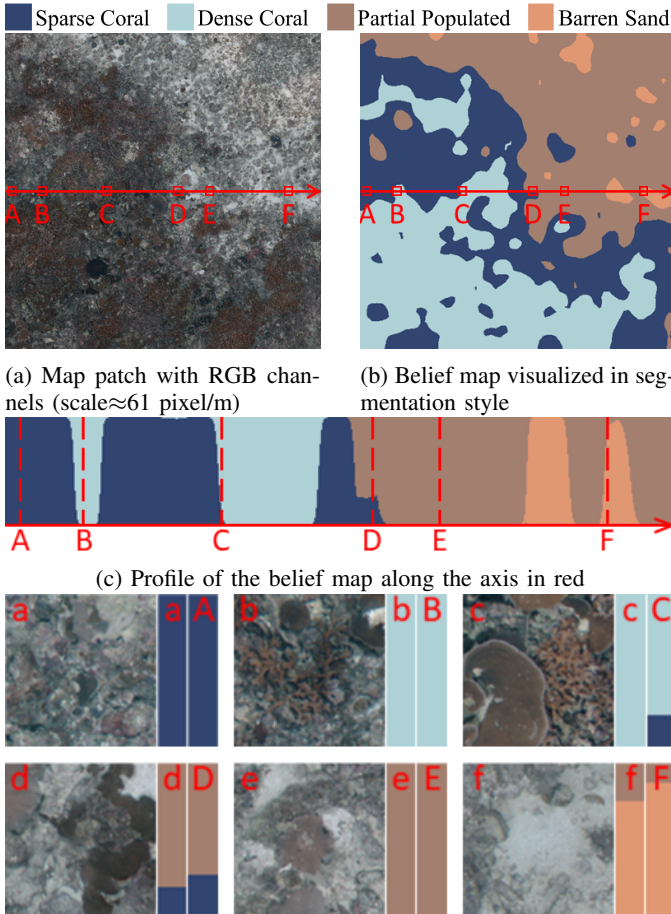
We use  $\tau = 1$  for loss function in presenting the results, which is selected empirically.

In our image augmentation family, we use the  $C_4$  [27] (the finite, cyclic, symmetry group of multiples of  $90^\circ$  rotations) for learning rotation-invariant representations. We also apply random changes in brightness, contrast, saturation, and hue.

The network is trained with SGD optimizer with momentum [35] for 300 epochs. The learning rate starts at 0.002, and is reduced by a factor of 0.1 once learning stagnates. We include 8 data tuples in a mini-batch, and each data tuple contains 6 image observations. In other words, a mini-batch contains 8 map patches and 48 image observations, which is the largest that fits in a 12GB GPU.

### C. Visualizations

We visualize the representations learned by both backbones to show that they learn consistent representations, see Fig. 4 and Fig. 5. Learned representations are colored channel-wise. Fig. 4a shows an RGB map patch from the Scott Reef dataset. Fig. 4b presents the belief map in segmentation style by performing *argmax* operation along the channel dimension. As shown in 4 different colors, the map patch is encoded into 4 different types of representations. The segmentation-style map shows a terrain pattern that generally aligns with the raw RGB map. Fig. 4c profiles the belief map along the axis in red. We can observe changes in 4 types of representations along the axis. This profile also reveals a sparse data structure in the belief map, where one channel dominates and the rest have values all close to 0. Such sparsity guarantees us the potential of compressing the belief map into a compact size. We compare the representations encoded from image observation and map in Fig. 4d. The positions where the image observations are located are also indicated in the Fig. 4a, 4b and 4c. From the comparison we see both encoders learn similar representations across scales. We also find that those



(a) Map patch with RGB channels (scale  $\approx 61$  pixel/m) (b) Belief map visualized in segmentation style

(c) Profile of the belief map along the axis in red

(d) Image observations (scale  $\approx 500$  pixel/m) and representations, labelled with **a-f**. Corresponding representations extracted from belief map are labelled with **A-F**.

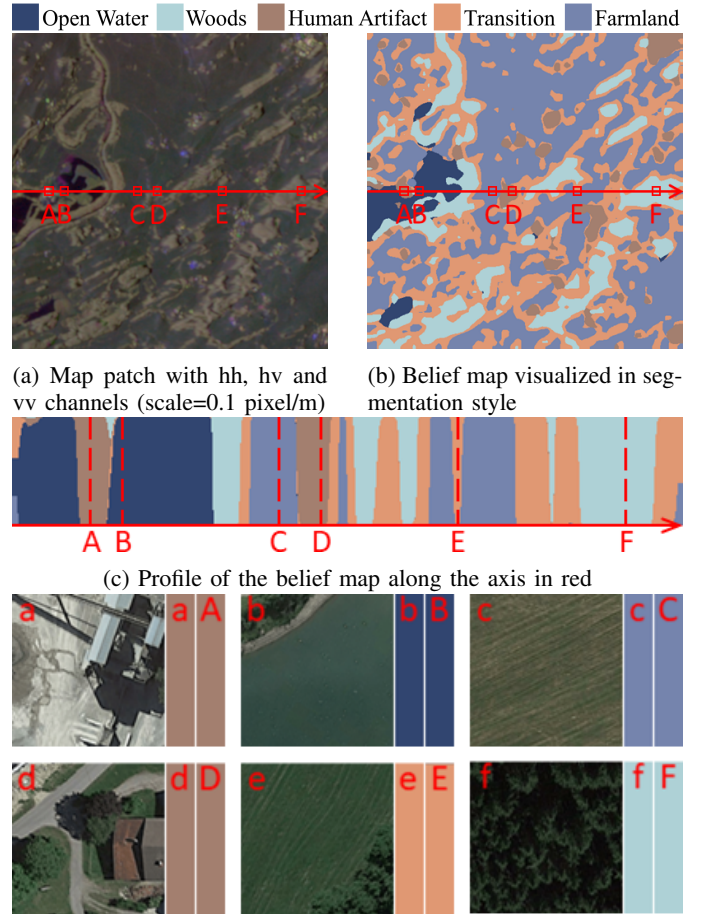
Fig. 4: Visualized representations for Scott Reef dataset. The legend on the top interprets each active channel in learned representations into 4 categories: sparse coral (a/A), dense coral (b/B and c/C), partial populated substrate (d/D and e/E) and barren sand (f/F). Note that both d/D and f/F are combinations of two types of terrains as represented.

representations learned without supervision can be interpreted into description with human oversight, including sparse/dense coral, partial populated substrate and barren sand (see legend on the top of Fig. 4). We do the same visualization for Kempton dataset (Fig. 5). In this patch, we see 5 different kinds of terrains represented: open water, woods, human artifacts, transition area and farmland (see legend on the top of Fig. 5).

We evaluate the probability density of image observation with each pixel in the belief map by Eq. 3 (with  $\theta = 5$ ), and visualize as a heat map (Fig. 6 and Fig. 7). The arrows indicate the ground truth position of image observations in the map. We can see that the images presented all lie in the area with deep red color indicating a high probability density.

#### D. Numerical Evaluation and Comparisons

We compare our approach with Triplet Network [18] and CVM-Net I [19]. To keep the comparison fair, we also experi-



(a) Map patch with hh, hv and vv channels (scale = 0.1 pixel/m) (b) Belief map visualized in segmentation style

(c) Profile of the belief map along the axis in red

(d) Image observations (scale  $\approx 7$  pixel/m) and representations, labelled with **a-f**. Corresponding representations extracted from belief map are labelled with **A-F**.

Fig. 5: Visualized representations for Kempton dataset. The legend on the top interprets each active channel in learned representations into 5 categories: human artifacts (a/A and d/D), open water area (b/B), farmland (c/C), transition area (e/E), and woods (f/F).

mented with their backbone replaced with ResNet18, which is identical to our image encoder (without the *softmax* layer). Since the other approaches all need image pairs from both scales for training and a sliding window search for testing, we sampled small-scale image tiles with resolution  $32 \times 32$  from the raw map. We choose this resolution because it will cover approximately the same (or larger) field of view (FOV) under the scale ratio and the performances of backbone networks are proven on datasets with  $32 \times 32$  resolution, e.g. CIFAR-10 [36].

1) *Recall*: We first investigate top- $k\%$  recall rate following [18], [19]. A higher recall rate means that the ground truth location is more likely to be included in the area with top- $k\%$  response as inferred. Since we expect our approach to work in conjunction with other localization frameworks as opposed to alone, we evaluate the recall rate on each map patch from the testing set, instead of the whole region of interest. The recall at 1% and 5% are reported in Table I. Our approach shows second to highest recall performance on Scott Reef dataset and the highest on Kempton dataset. It is worth mention that, the

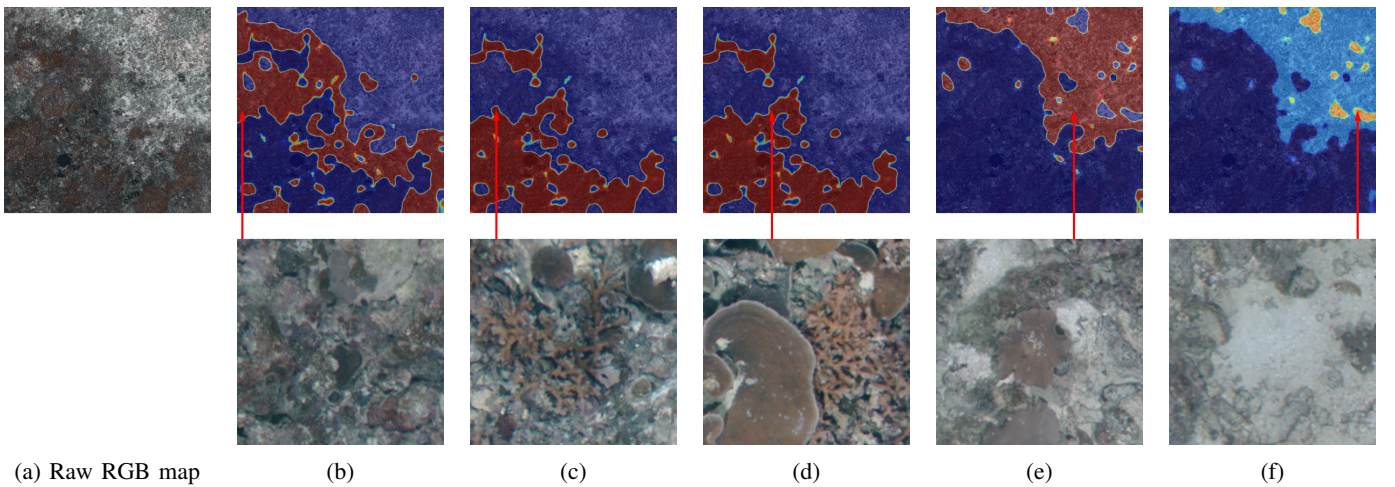


Fig. 6: Scott Reef Dataset: locations of image observations inferred in the map

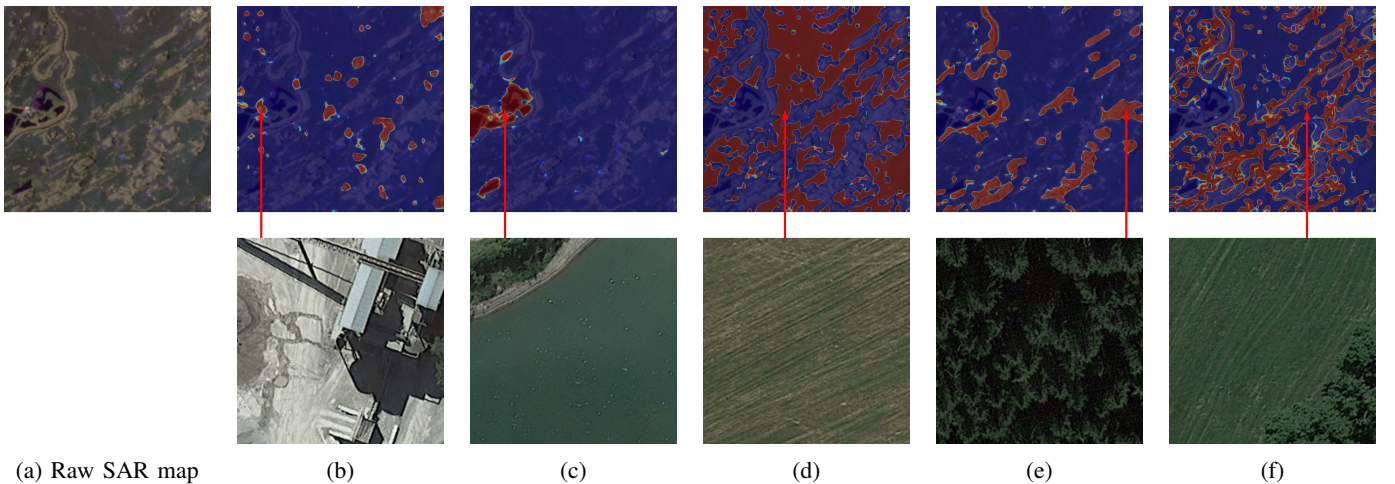


Fig. 7: Kempton Dataset: locations of image observations inferred in the map

	Scott Reef		Kempton	
	1%	5%	1%	5%
Triplet [18]	7.11%	13.92%	18.10%	22.40%
Triplet (ResNet18)	<b>63.86%</b>	<b>66.98%</b>	34.91%	37.56%
CVM-Net [19]	29.48%	51.31%	33.61%	38.66%
CVM-Net (ResNet18)	27.27%	48.85%	24.48%	34.42%
Ours	51.92%	56.35%	<b>35.81%</b>	<b>40.28%</b>

TABLE I: Comparison by average recall rate

scale ratio between image observation and the map patch is  $\times 8$  for Scott Reef, while approximately  $\times 70$  for Kempton. The results above imply that as the scale ratio gets larger, it's harder to extract and associate local features across scales. Since our approach observes the map as a whole instead of with a local sliding window, it seems to be the least downgraded approach regarding the recall rate.

2) *Synthetic trajectory*: Comparing to the urban environments studied in [18]–[20], features in nature are more repetitive. Particularly in small-scale maps, the network learns similar representations for terrains with the same appearances. Hence we do not report any precision metrics which heavily

depend on the unequal coverage of each terrain type. Instead, we directly evaluate how effective the learned representations are in state estimation with synthetic trajectories. We implemented the particle filter based on a TAN framework [4] which corrects the state estimation every time an image observation comes in. Instead of simulating the vehicle dynamics, we generate a straight-line 2D trajectory and add Gaussian noise in the incremental estimations. We randomly generate 100 noisy sequences aiming to evaluate the average improvement in localization with particle filtering. The likelihood function in TAN is realized with Eq. 4. For other approaches in comparison, we use the *softmax* of cosine similarity to update the particle weights. We experimented on 5 map patches selected with variations in terrain appearance from each dataset.

We visualize the particle filtering on selected patch 1 from each of both datasets in Fig. 8. We see that for both patches, estimation errors along the trajectory are generally reduced with particle filtering, which means that our proposed network learns an effective representation for inference across the scale ratio and modality gap. However, from the visualization, we also observe certain outlying sequences not converging to

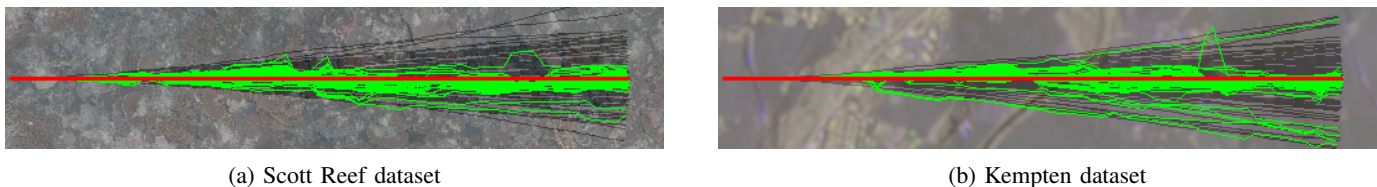


Fig. 8: Running particle filter on selected map patches. The groundtruth trajectory, noisy estimations and filtered estimations are plotted in red, grey and green respectively. The trajectory propagates from left to right.

	Scott Reef					Kempton				
	Patch 1	Patch 2	Patch 3	Patch 4	Patch 5	Patch 1	Patch 2	Patch 3	Patch 4	Patch 5
Triplet [18]	-5.2%	1.3%	-1.8%	-13.3%	-1.1%	5.1%	6.5%	12.3%	6.6%	25.4%
Triplet (ResNet18)	45.7%	<b>33.2%</b>	18.4%	12.1%	8.1%	31.1%	19.13%	22.8%	0.1%	13.3%
CVM-Net [19]	-5.6%	21.7%	9.3%	-0.2%	23.0%	30.2%	30.9%	23.2%	28.15%	<b>44.91%</b>
CVM-Net (ResNet18)	23.9%	8.5%	<b>31.5%</b>	7.0%	14.6%	43.3%	15.8%	13.1%	<b>29.4%</b>	22.9%
Ours	<b>58.4%</b>	18.5%	25.7%	<b>25.05%</b>	<b>25.09%</b>	<b>46.6%</b>	<b>37.9%</b>	<b>28.2%</b>	15.4%	19.9%

TABLE II: Error reduction on selected map patches. Negative values in grey mean that the error is increased.

	Computation Time	GPU Memory Consumption	Belief Map Size (Theoretical)	Belief Map Size (in 32-bit float point)
Triplet [18]	220.67 s	1.97 Gb	$m \cdot c$	<b>5.01 Mb</b>
Triplet (ResNet18)	587.19 s	1.61 Gb	$m \cdot c$	<b>5.01 Mb</b>
CVMNet [19]	1054.63 s	1.13 Gb	$m \cdot c \cdot d$	2560.06 Mb
CVMNet (ResNet18)	1770.64 s	1.70 Gb	$m \cdot c \cdot d$	2560.06 Mb
Ours	<b>53.81 s</b>	<b>1.05 Gb</b>	$m \cdot c$	<b>5.01 Mb</b>

TABLE III: Computational efficiency:  $m$ ,  $c$ , and  $d$  are the size of the belief map, channels and descriptors respectively.

ground truth trajectory. The reason behind this can be the inconsistent representation pushing the estimation away from the true trajectory. Also, with no variation in observation nor map, particle filtering is only adding uncertainty into the system. In such cases, the drift is exaggerated, raising the concern about deployment in real environments.

The correction performances by particle filtering on all selected map patches are presented in Table II. For each sequence, we use the accumulated L2 error as the evaluation metric. To eliminate outliers, we report the median accumulated error among all the sequences for each map patch instead of the average error. It can be seen that our approach outperforms other approaches on three trajectories out of five on both datasets. As the particle filter usually has unpredictable performance with different maps or trajectories, we notice that our approach is one of the most stable which reduced average error by 15% – 60% on all selected patches.

3) *Computational cost and efficiency*: Computation resource consumption of encoding a single map patch is presented in Table III. The experiment is conducted on a Jetson Nano computer with 2Gb memory in MAXN power mode. Our approach is the most efficient regarding the time and memory consumed. It is because other approaches conduct sliding window search which process a large batch of image tiles in parallel, while our approach takes the whole map patch as input. Given the limited travelling speed of a mapping robot, our time consumption which is less than 1 minute per map patch promises real-time map encoding. The belief map size of our approach is the same compact size as that of Triplet network. CVM-Net uses a high dimensional descriptor

for deep features of each category, hence the map size is multiplied by descriptor size. The compact map size of our approach enables the potential application with real-time map streaming over the network.

## VI. CONCLUSIONS

In our proposed cross-scale geo-localization task, we break the limitations of existing studies which rely on large-scale high-resolution satellite images as maps. Instead, we extend the range of modalities that can serve as a map in geo-localization. We build two datasets from two domains, underwater and aerial, across different modalities and platforms. On both datasets, our proposed framework demonstrates the ability to learn consistent representations from image observations and maps. Especially, our approach managed to deal with the significant scale ratio between them. In contrast to previous studies, we move away from the paradigm of image retrieval and exhaustive search. We encode a map patch into a belief map, which results in the best computation efficiency regarding time, memory, and storage consumption. Such properties make our approach a solution where a map needed to be updated in real-time. We also believe that for small-scale maps, a pixel-wise encoder looking at the whole map is better at extracting and corresponding features across the scales, which is evidenced by the comparison on recall rate. Experiments with synthetic trajectories show that representations learned with our approach are the most effective in localization. Also, the probabilistic nature of our cross-scale representation makes it compatible as a plug-in module in state estimation pipelines.

This study overall provides an idea for localizing a perceptual robot in the field with a map. To train the system to

describe the map and observations with abstract “language”, what we need is just image observations tagged with 2D geospatial locations in the map. No labelling is needed at all as our approach is based on contrastive learning. For subsea applications where geo-tags are absent, we have demonstrated how to generate dataset from underwater survey data and train the network in the map’s local geo-coordinate.

However, a belief map with 5Mb size is still heavy for low-bandwidth networks, e.g. underwater acoustic communication. In the future study, we will be interested in compressing the belief map using its sparsity for efficient map transmitting, and demonstrate this work on real robots.

## ACKNOWLEDGEMENTS

We gratefully acknowledge the Australian Centre for Field Robotics’ Marine Robotics Group for providing the data.

## REFERENCES

- [1] T. Qin, S. Cao, J. Pan, and S. Shen, “A general optimization-based framework for global pose estimation with multiple sensors,” *ArXiv*, vol. abs/1901.03642, 2019.
- [2] A. Bhattacharyya, “On a measure of divergence between two multinomial populations,” *Sankhyā: the indian journal of statistics*, pp. 401–406, 1946.
- [3] T. Chen, S. Kornblith, M. Norouzi, and G. Hinton, “A simple framework for contrastive learning of visual representations,” *arXiv preprint arXiv:2002.05709*, 2020.
- [4] R. Karlsson and F. Gustafsson, “Particle filter for underwater terrain navigation,” in *IEEE Workshop on Statistical Signal Processing, 2003*, 2003, pp. 526–529.
- [5] F. Maurelli, S. Krupinski, Y. Petillot, and J. Salvi, “A particle filter approach for auv localization,” in *OCEANS*, 2008.
- [6] J. Jung, J. Park, J. Choi, and H.-T. Choi, “Terrain based navigation for an autonomous surface vehicle with a multibeam sonar,” in *OCEANS 2019 - Marseille*, 2019, pp. 1–4.
- [7] D. K. Meduna, S. M. Rock, and R. McEwen, “Low-cost terrain relative navigation for long-range auvs,” in *OCEANS*, 2008.
- [8] F. C. Teixeira, J. Quintas, P. Maurya, and A. Pascoal, “Robust particle filter formulations with application to terrain-aided navigation,” *International Journal of Adaptive Control and Signal Processing*, vol. 31, no. 4, pp. 608–651, 2017.
- [9] D. Peng, T. Zhou, C. xu, W.-y. Zhang, and J. Shen, “Marginalized point mass filter with estimating tidal depth bias for underwater terrain-aided navigation,” *Journal of Sensors*, vol. 2019, pp. 1–15, May 2019.
- [10] N. Fairfield, G. Kantor, and D. Wettergreen, “Towards particle filter slam with three dimensional evidence grids in a flooded subterranean environment,” in *IEEE International Conference on Robotics and Automation (ICRA)*, 2006, pp. 3575–3580.
- [11] S. Barkby, S. Williams, O. Pizarro, and M. Jakuba, “An efficient approach to bathymetric slam,” in *2009 IEEE/RSJ International Conference on Intelligent Robots and Systems*, 2009, pp. 219–224.
- [12] S. Barkby, S. B. Williams, O. Pizarro, and M. V. Jakuba, “A featureless approach to efficient bathymetric slam using distributed particle mapping,” *Journal of Field Robotics*, vol. 28, no. 1, pp. 19–39, 2011.
- [13] Y. T. Tan, M. Chitre, and F. S. Hover, “Cooperative bathymetry-based localization using low-cost autonomous underwater vehicles,” *Autonomous Robots*, vol. 40, no. 7, pp. 1187–1205, 2016.
- [14] A. Wiktor and S. Rock, “Collaborative multi-robot localization in natural terrain,” in *IEEE International Conference on Robotics and Automation (ICRA)*, 2020, pp. 4529–4535.
- [15] J. Anderson and G. Hollinger, “Communication planning for cooperative terrain-based underwater localization,” *Sensors*, vol. 21, p. 1675, Mar. 2021.
- [16] T.-Y. Lin, S. Belongie, and J. Hays, “Cross-view image geolocalization,” in *2013 IEEE Conference on Computer Vision and Pattern Recognition*, 2013, pp. 891–898.
- [17] S. Workman, R. Souvenir, and N. Jacobs, “Wide-area image geolocalization with aerial reference imagery,” in *ICCV*, 2015, pp. 3961–3969.
- [18] N. N. Vo and J. Hays, “Localizing and orienting street views using overhead imagery,” in *European conference on computer vision*, Springer, 2016, pp. 494–509.
- [19] S. Hu, M. Feng, R. M. H. Nguyen, and G. H. Lee, “Cvmnet: Cross-view matching network for image-based ground-to-aerial geo-localization,” in *IEEE/CVF Conference on Computer Vision and Pattern Recognition*, 2018, pp. 7258–7267.
- [20] R. Arandjelović, P. Gronat, A. Torii, T. Pajdla, and J. Sivic, “Netvlad: Cnn architecture for weakly supervised place recognition,” *IEEE Transactions on Pattern Analysis and Machine Intelligence*, vol. 40, no. 6, pp. 1437–1451, 2018.
- [21] K. Regmi and M. Shah, “Bridging the domain gap for ground-to-aerial image matching,” in *2019 IEEE/CVF International Conference on Computer Vision (ICCV)*, 2019, pp. 470–479.
- [22] Y. Shi, L. Liu, X. Yu, and H. Li, “Spatial-aware feature aggregation for image based cross-view geo-localization,” in *NeurIPS*, 2019.
- [23] Y. Shi, X. Yu, D. Campbell, and H. Li, “Where am i looking at? joint location and orientation estimation by cross-view matching,” *2020 IEEE/CVF Conference on Computer Vision and Pattern Recognition (CVPR)*, pp. 4063–4071, 2020.
- [24] R. Cao, J. Zhu, W. Tu, Q. Li, J. Cao, B. Liu, Q. Zhang, and G. Qiu, “Integrating aerial and street view images for urban land use classification,” *Remote Sensing*, vol. 10, no. 10, 2018.
- [25] D. Hong, L. Gao, N. Yokoya, J. Yao, J. Chanussot, Q. Du, and B. Zhang, “More diverse means better: Multimodal deep learning meets remote-sensing imagery classification,” *IEEE Transactions on Geoscience and Remote Sensing*, vol. 59, no. 5, pp. 4340–4354, 2020.
- [26] K. He, H. Fan, Y. Wu, S. Xie, and R. Girshick, “Momentum contrast for unsupervised visual representation learning,” in *CVPR*, 2020, pp. 9729–9738.
- [27] N. Pielawski, E. Wetzter, J. Öfverstedt, J. Lu, C. Wählby, J. Lindblad, and N. Sladoje, “CoMIR: Contrastive multimodal image representation for registration,” in *NeurIPS*, 2020.
- [28] F. Dellaert, “Factor graphs and gtsam: A hands-on introduction,” Georgia Institute of Technology, Tech. Rep., 2012.
- [29] D. M. Steinberg, S. B. Williams, O. Pizarro, and M. V. Jakuba, “Towards autonomous habitat classification using gaussian mixture models,” in *2010 IEEE/RSJ International Conference on Intelligent Robots and Systems*, 2010, pp. 4424–4431.
- [30] M. Ferrera, V. Creuze, J. Moras, and P. Trouvé-Peloux, “Aqualoc: An underwater dataset for visual–inertial–pressure localization,” *The International Journal of Robotics Research*, vol. 38, no. 14, pp. 1549–1559, 2019.
- [31] *Google Earth Engine*, <https://developers.google.com/earth-engine>, accessed 2021-02-01.
- [32] *Google Map Static API*, <http://developers.google.com/maps/documentation/maps-static/overview>, accessed 2021-02-01.
- [33] J. Long, E. Shelhamer, and T. Darrell, “Fully convolutional networks for semantic segmentation,” in *CVPR*, 2015, pp. 3431–3440.
- [34] K. He, X. Zhang, S. Ren, and J. Sun, “Deep residual learning for image recognition,” in *IEEE conference on computer vision and pattern recognition*, 2016, pp. 770–778.
- [35] I. Sutskever, J. Martens, G. Dahl, and G. Hinton, “On the importance of initialization and momentum in deep learning,” in *International conference on machine learning*, PMLR, 2013, pp. 1139–1147.

- [36] A. Krizhevsky, "Learning multiple layers of features from tiny images," 2009.